

This is the accepted manuscript made available via CHORUS, the article has been published as:

Effects of transfer channels on near- and sub-barrier fusion of $^{32}\text{S} + ^{48}\text{Ca}$

G. Montagnoli, A. M. Stefanini, H. Esbensen, C. L. Jiang, L. Corradi, S. Courtin, E. Fioretto, A. Goasduff, J. Grebosz, F. Haas, M. Mazzocco, C. Michelagnoli, T. Mijatovic, D. Montanari, C. Parascandolo, K. E. Rehm, F. Scarlassara, S. Szilner, X. D. Tang, and C. A. Ur

Phys. Rev. C **87**, 014611 — Published 22 January 2013

DOI: [10.1103/PhysRevC.87.014611](https://doi.org/10.1103/PhysRevC.87.014611)

Effects of transfer channels on near- and sub-barrier fusion of $^{32}\text{S}+^{48}\text{Ca}$

G. Montagnoli¹, A.M. Stefanini², H.Esbensen³, C.L.Jiang³, L. Corradi², S. Courtin⁴, E. Fioretto², A. Goasduff⁴, J.Grebosz⁵, F. Haas⁴, M.Mazzocco¹, C.Michelagnoli¹, T. Mijatovic⁶, D.Montanari¹, C.Parascandolo¹, K.E.Rehm³, F. Scarlassara¹, S. Szilner⁶, X.D.Tang⁷, C.A.Ur¹

¹ *Dipartimento di Fisica e Astronomia, Università di Padova,
and INFN, Sez. di Padova, I-35131 Padova, Italy*

² *INFN, Laboratori Nazionali di Legnaro, I-35020 Legnaro (Padova), Italy*

³ *Physics Division, Argonne National Laboratory, Argonne, IL 60439, USA*

⁴ *IPHC, CNRS-IN2P3, Université de Strasbourg, F-67037 Strasbourg Cedex 2, France*

⁵ *Institute of Nuclear Physics, Polish Academy of Sciences, PL 31-342 Cracow, Poland*

⁶ *Ruđer Bošković Institute, HR-10002 Zagreb, Croatia*

⁷ *University of Notre Dame, Notre Dame, IN 46556, USA*

(Dated: January 7, 2013)

The fusion excitation function of $^{32}\text{S} + ^{48}\text{Ca}$ has been experimentally studied in a wide energy range, from above the Coulomb barrier down to cross sections in the sub- μb region. The measurements were done at INFN-Laboratori Nazionali di Legnaro, using the ^{32}S beam from the XTU Tandem accelerator. The excitation function has a smooth behavior below the barrier, and no evident hindrance character shows up in the measured energy region. The fusion barrier distribution has a peculiar shape with two distinct peaks of similar height, lower and higher than the Akyüz-Winther barrier. Coupled-channels calculations using the M3Y + repulsion potential are presented for this system and for $^{36}\text{S}+^{48}\text{Ca}$. The results of these calculations give a good account of the data, and indicate the influence of one- and two-nucleon transfer channels with positive Q -values, which are only open for $^{32}\text{S} + ^{48}\text{Ca}$.

PACS Numbers: 25.70.Jj, 24.10.Eq

I. INTRODUCTION

The influence of nucleon transfer couplings on heavy-ion fusion near the Coulomb barrier has been much debated since the early fusion experiment for $^{58}\text{Ni}+^{64}\text{Ni}$ by Beckerman et al. [1, 2] which showed a strong unexpected enhancement with respect to the fusion of the two symmetric systems, $^{58}\text{Ni}+^{58}\text{Ni}$ and $^{64}\text{Ni}+^{64}\text{Ni}$. It was suggested by Broglia et al. [3] that the couplings to transfer channels with positive Q -values can explain the enhancement of the fusion in the asymmetric $^{58}\text{Ni}+^{64}\text{Ni}$ system. We have recently observed the same phenomenon in the fusion of calcium isotopes [4]. There, the fusion of the asymmetric $^{40}\text{Ca}+^{48}\text{Ca}$ system [5] is enhanced at sub-barrier energies compared to the fusion of the two symmetric systems $^{40}\text{Ca}+^{40}\text{Ca}$ and $^{48}\text{Ca}+^{48}\text{Ca}$, whereas it is suppressed at energies above the Coulomb barrier. We showed that it is possible to explain the fusion data for $^{40}\text{Ca}+^{48}\text{Ca}$ by adjusting the coupling to two-nucleon transfer channels. The necessary coupling strength has not been tested directly because the cross sections for pair-transfer (two-proton or two-neutron) have not yet been measured.

There are many other systems for which the sub-barrier fusion is expected to be enhanced due to the influence of one- and two-nucleon transfer channels with positive Q -values. These include measurements at Legnaro, for example, of the fusion of different calcium and zirconium isotopes [6, 7], and of sulphur plus nickel isotopes [8–10]. A further recent example is reported in Ref. [11].

In this work we analyze the fusion of two sulphur iso-

topes with ^{48}Ca . The fusion of $^{32}\text{S} + ^{48}\text{Ca}$ is reported here for the first time, whereas the fusion of $^{36}\text{S}+^{48}\text{Ca}$ was measured a few years ago [12]. Preliminary results of the $^{32}\text{S} + ^{48}\text{Ca}$ measurements have been outlined at recent Conferences [13, 14], as well as a first theoretical approach, where the couplings to transfer channels were treated schematically. In this paper, the final data are presented in detail, together with a more complete theoretical analysis.

Actually, all of the one- and two-nucleon transfer channels in $^{36}\text{S}+^{48}\text{Ca}$ collisions have negative Q -values, whereas the two-neutron, one-proton and two-proton transfer channels in $^{32}\text{S}+^{48}\text{Ca}$ collisions have positive ground state Q -values. We will therefore first analyze the $^{36}\text{S}+^{48}\text{Ca}$ fusion data and consider the effect of couplings to inelastic excitations in the coupled-channels (CC) calculations, while ignoring transfer couplings. The analysis will help getting some handle on the ion-ion potential, which here is the M3Y+repulsion, double-folding potential [15], and this will also put some constraints on the ion-ion potential for $^{32}\text{S}+^{48}\text{Ca}$. We shall see that it is possible to develop a good description of the fusion data for the latter system by including couplings to one- and two-nucleon transfer channels and by adjusting the strength and the effective Q -value of the pair-transfer.

II. EXPERIMENTAL

The fusion excitation function of $^{32}\text{S} + ^{48}\text{Ca}$ has been measured at INFN - Laboratori Nazionali di Legnaro (LNL), using the high-quality and intense ^{32}S beam (up

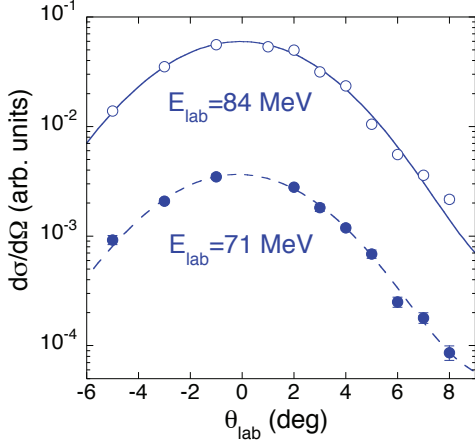


FIG. 1: (Color online) Angular distributions measured at two different energies near the Coulomb barrier together with Gaussian fits. Only statistical errors are reported, not exceeding the symbol size in most cases.

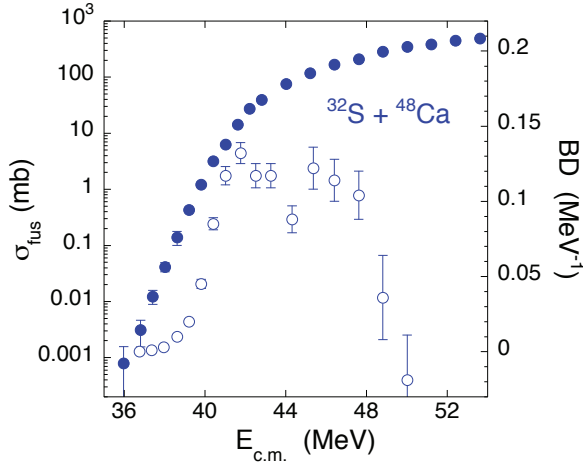


FIG. 2: (Color online) Fusion excitation function (full symbols, left scale) and extracted barrier distribution (open symbols, right scale) for $^{32}\text{S} + ^{48}\text{Ca}$. Plotted errors are purely statistical.

to $\simeq 30$ pA) from the XTU Tandem accelerator, at laboratory energies in the range 60.0–89.4 MeV. The targets were $50\mu\text{g}/\text{cm}^2$ evaporations of $^{48}\text{CaF}_2$ onto $15\mu\text{g}/\text{cm}^2$ carbon backings.

The beam energy losses in the targets were taken into account, as well as the calcium isotopic enrichment (96.56% in mass 48), with a predominant 3.17% impurity of ^{40}Ca . The barrier for $^{32}\text{S} + ^{48}\text{Ca}$ is $\simeq 9$ MeV lower with respect to $^{32}\text{S} + ^{40}\text{Ca}$, in the laboratory system. The impurity of ^{46}Ca is $< 0.01\%$ with a barrier difference of $\simeq 2$ MeV. All this produces small or even negligible corrections in the whole sub-barrier energy range. As for possible target contaminants with $Z < 20$, the mass of the corresponding compound nuclei are very different, so that the fusion-evaporation residues would have been easily separated out by the combined energy-time-of-flight

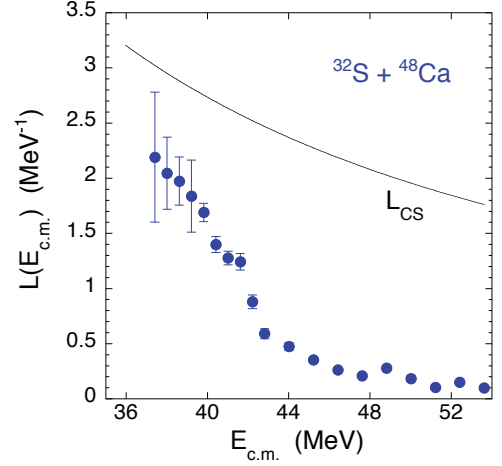


FIG. 3: (Color online) Logarithmic slope and the L_{CS} limit (solid line), see text.

measurements described below.

Since fusion-fission is negligible for $^{32}\text{S} + ^{48}\text{Ca}$ in the considered energy range, the fusion cross section was obtained by detecting at forward angles the evaporation residues (ER) following compound nucleus formation. The ER were separated from the beam by using the set-up based on an electrostatic deflector (see [4] and Refs. therein) employed specifically for these kind of measurements at LNL. The set-up is simple to operate, can rotate around the target position to measure ER angular distributions and its transmission can be determined by comparing the ER yields with electric field on and off.

Two large-size micro-channel plate detectors (MCP) $30 \times 50 \text{ mm}^2$ and a transverse-field ionization chamber (IC) have been recently added to the original set-up [16], in the detector telescope downstream the deflector. In this upgraded configuration, the ER are detected by the two MCP, enter the IC giving an energy loss signal ΔE and are finally stopped in a circular 600 mm^2 silicon detector placed in the same gas (CH_4) volume. The silicon detector provides the residual energy (E) and the start signal used for the two independent time-of-flights (TOF), and for triggering the data acquisition. The total length of the detector telescope is $\simeq 105$ cm, and the geometrical solid angle of the whole set-up in the present experiment was $41.3 \pm 0.3 \mu\text{sr}$. This was determined by the silicon detector size and was measured with an α -source at the target position.

Four silicon detectors were used for beam monitoring and normalization between the different runs, by measuring the Rutherford scattering from the target. They were placed at the same scattering angle $\theta_{lab} = 16^\circ$, above and below, and to the left and right of the beam direction, at around 300 mm from the target. ER angular distributions were measured at $E_{lab} = 70.4$, and 83.4 MeV in the range 0° to 8° , and are shown in Fig. 1.

Total fusion cross sections were derived from the normalized ER yields obtained at 0° or 2° (depending on

beam background conditions), from the ER angular distributions, and from the transmission of the electrostatic deflector $T=0.72\pm0.04$, derived from systematic measurements performed for systems with nearby masses and/or mass asymmetries, in particular $^{36}\text{S}+^{48}\text{Ca}$ [12]. The absolute cross section scale is estimated to be accurate within $\pm 8\%$, summing up the uncertainties arising from the detector solid angles, from the fits of the angular distributions, and from the transmission of the electrostatic deflector. Statistical errors are 2–3% near and above the barrier, and become much larger at low energies where few fusion events were detected.

III. SURVEY OF RESULTS

The measured fusion excitation function of $^{32}\text{S}+^{48}\text{Ca}$ is shown in Fig. 2. It is evident that the cross sections decrease very smoothly below the barrier. The lowest-measured cross section is $\simeq 800$ nb. This seemingly structureless excitation function hides, however, a barrier distribution with interesting features. This has been extracted with the usual three-point formula [17] and an energy step of $\Delta E_{cm} \simeq 1.8$ MeV. Fig. 2 shows that the barrier distribution is very wide (around 8 MeV) and that two peaks of similar height show up, on either side of the Akyüz-Winther (AW) [18] unperturbed barrier at $E_{cm} = 43.4$ MeV.

Fig. 3 shows the logarithmic slope of the excitation function, derived from the measured cross sections, as the incremental ratio of two nearby points. In the measured energy range, the slope increases steadily below the barrier with decreasing energy with no notable irregularity. It does not reach the value expected for a constant astrophysical S factor (L_{CS} in Fig. 3), which implies, by the way, that no maximum of S vs. energy shows up [19].

According to the phenomenological systematics of Jiang [20, 21] for stiff systems, the threshold for fusion hindrance would be expected at ≈ 40 MeV. Our measurements extend almost 4 MeV below, and, qualitatively speaking, no evidence of hindrance shows up. Obviously, it might appear at still lower energies for $^{32}\text{S}+^{48}\text{Ca}$ (which cannot be considered stiff). The comparison with the CC calculations we are going to present in the next Section, and the comparison with $^{36}\text{S}+^{48}\text{Ca}$, will tell us more about this point.

IV. THE COUPLED-CHANNELS APPROACH

The CC equations are solved in the rotating-frame approximation with scattering boundary conditions at large radial separations of the colliding nuclei, that is, with an ingoing wave in the elastic channels and outgoing waves in all channels. Furthermore, ingoing-wave boundary conditions are imposed at the minimum of the pocket in the entrance channel potential for each angular momentum L . The partial fusion cross section is then

TABLE I: Adopted structure of the excited states in ^{48}Ca [28, 29], ^{32}S [29, 30] and ^{36}S [29, 31]. ^{32}S is treated as a deformed nucleus with deformation parameter $\beta_2 = 0.315$ (see text). The last two columns report the Coulomb and nuclear deformation lengths, respectively.

	λ^π	$E_x(\text{MeV})$	$B(E\lambda)_{Wu}$	β_λ^C	$\sigma_\lambda^C(\text{fm})$	$\sigma_\lambda^N(\text{fm})$
^{48}Ca	2^+	3.832	1.71(9)	0.102	0.126	0.190
	$2\text{PH}(2^+)$	4.849	4.7(29)	0.082	0.15	0.15
	3^-	4.507	5.0(8)	0.203	0.250	0.190
	5^-	5.146		0.040	0.049	0.038
^{32}S	2^+	2.230	10.0(4)	0.315	0.339	0.339
	$2\text{PH}(2^+)$	4.288	11.8(12)	0.244	0.262	0.262
	3^-	5.006	16(3)	0.391	0.420	0.420
^{36}S	2^+	3.291	2.83(24)	0.166	0.186	0.186
	3^-	4.193	15(5)	0.376	0.420	0.420

TABLE II: Parameters of the M3Y+repulsion interaction that give the best fit to the $^{36}\text{S}+^{48}\text{Ca}$ [12] and $^{32}\text{S}+^{48}\text{Ca}$ fusion data, respectively. The second column shows the extracted matter radii of the two sulphur isotopes. The parameter a_r described in the text was determined from the best fits to the $^{36}\text{S}+^{48}\text{Ca}$ fusion data. Only the results of the second solution Sol-2 are considered in the text, and the value of $a_r = 0.427$ fm is adopted for $^{32}\text{S}+^{48}\text{Ca}$. The Table also shows the energy of the pocket, V_{min} , and the height of the Coulomb barrier V_{CB} . The last column reports the best value of the χ^2/N obtained with a systematic error of 5%.

	$R(\text{fm})$	$a_r(\text{fm})$	$V_{min}(\text{MeV})$	$V_{CB}(\text{MeV})$	χ^2/N
^{36}S Sol-1	3.055	0.375	15.94	42.68	0.90
^{36}S Sol-2	3.142	0.427	25.57	42.66	0.81
^{32}S	2.83	0.427	26.02	43.81	1.41

obtained from the ingoing flux at the minimum of each L -dependent entrance channel potential.

A weak and short-ranged imaginary potential is also applied. It has the parametrization

$$W(L, r) = \frac{W_0}{1 + \exp((r - R_w(L))/a_w)}, \quad (1)$$

where $R_w(L)$ is the radial position of the pocket in the L dependent entrance channel potential, $W_0 = -5$ MeV, and $a_w = 0.2$ fm. The fusion cross section is then determined as the sum of the ingoing flux and the absorption by the imaginary potential. The weak imaginary potential eliminates some unwanted fluctuations in the calculated fusion cross section. It also provides a mechanism for fusion at energies far above the Coulomb barrier and at high angular momenta where the pocket in the entrance channel potential may disappear. At extreme sub-barrier energies it is preferable not to use any imaginary potential. The fusion will then vanish at energies below the minimum of the pocket in the entrance channel since the ingoing flux will be zero. This mechanism helps explain the fusion hindrance phenomenon which has been ob-

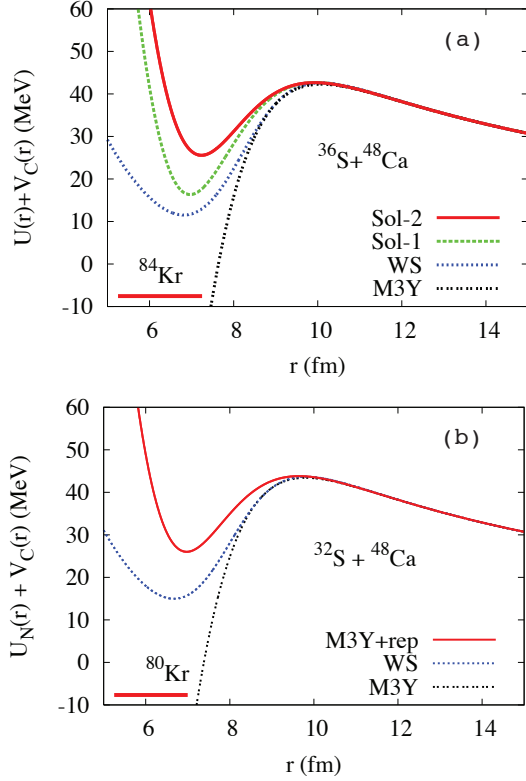


FIG. 4: (Color online) Top panel (a): the M3Y+repulsion entrance channel potentials (Sol-1, Sol-2) for the two stable solutions to the fusion of $^{36}\text{S} + ^{48}\text{Ca}$ are compared to the Woods-Saxon (WS) potential described in the text, and to the pure M3Y+exchange potential. Bottom panel (b): the corresponding potentials used for $^{32}\text{S} + ^{48}\text{Ca}$. The ground state energies of the two compound nuclei $^{84,80}\text{Kr}$ are indicated by the solid horizontal lines.

served in many systems [20].

The calculations are based on the M3Y+repulsion, double-folding potential [15]. The densities of the reacting nuclei are parametrized in terms of the symmetrized Fermi function, Eq. (4) of Ref. [22]. The diffuseness of the density that is used in calculating the ordinary M3Y double-folding potential is taken from electron scattering [25], whereas the diffuseness a_r of the densities associated with the repulsive part of the interaction (see Ref. [15] for details) is adjusted. The radius of the two types of densities is assumed to be the same. The radius of ^{48}Ca is taken from the analysis [22] of the $^{48}\text{Ca} + ^{48}\text{Ca}$ fusion experiment [26].

There are two adjustable parameters of the ion-ion potential, namely, the radius of the sulphur isotope considered and the diffuseness a_r associated with the repulsive interaction. The strength of the repulsion, on the other hand, is calibrated to produce the expected incompressibility of the compound nucleus [27]. The compound nucleus for $^{36}\text{S} + ^{48}\text{Ca}$ is ^{84}Kr which has a neutron excess of $\delta = (N-Z)/A = 1/7$ and an incompressibility of $K = 226.5$ MeV. The compound nucleus for $^{32}\text{S} + ^{48}\text{Ca}$ is ^{80}Kr with a neutron excess $\delta = 1/10$, and an incompressibility

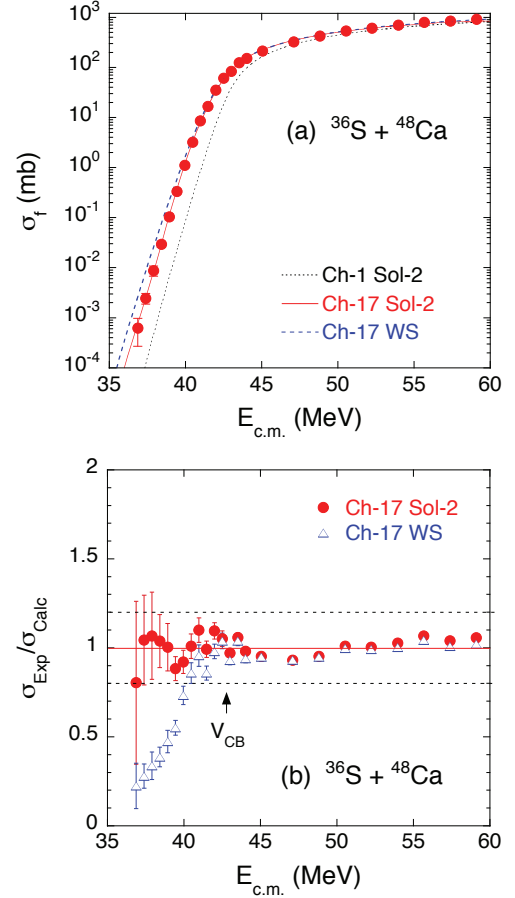


FIG. 5: (Color online) In the top panel (a) fusion cross sections for $^{36}\text{S} + ^{48}\text{Ca}$ [12] are compared to CC calculations (Ch-17) based on a WS potential, and on the M3Y+repulsion potential Sol-2. The no-coupling limit Ch-1 is also shown. The lower panel (b) reports the ratio of the measured and calculated cross sections, using the two potentials. The energy of the Coulomb barrier is indicated.

TABLE III: Density parameters. The radii of ^{48}Ca and ^{36}S were adjusted to optimize the fit to the fusion data of Refs. [26] and [12], respectively. The density parameters for ^{32}S were obtained in this work by analyzing the fusion data of $^{32}\text{S} + ^{48}\text{Ca}$. The rms radii of the densities are compared to the measured rms charge radii [32] and the associated point-proton (pp) rms radii. The last line includes the effect of deformation in ^{32}S .

Nucleus	R(fm)	a(fm)	rms	rms pp
^{36}S charge [32]			3.298(2)	3.204
Sol-1 [12]	3.055	0.563	3.159	
Sol-2 [12]	3.142	0.563	3.210	
^{48}Ca charge [32]			3.474(1)	3.387(1)
^{48}Ca Sol-2 [22]	3.80	0.54	3.563	
^{32}S charge [32]			3.261(2)	3.161
^{32}S $\beta_2=0$	2.83	0.56	3.02	
^{32}S $\beta_2=0.315$	2.83	0.56	3.06	

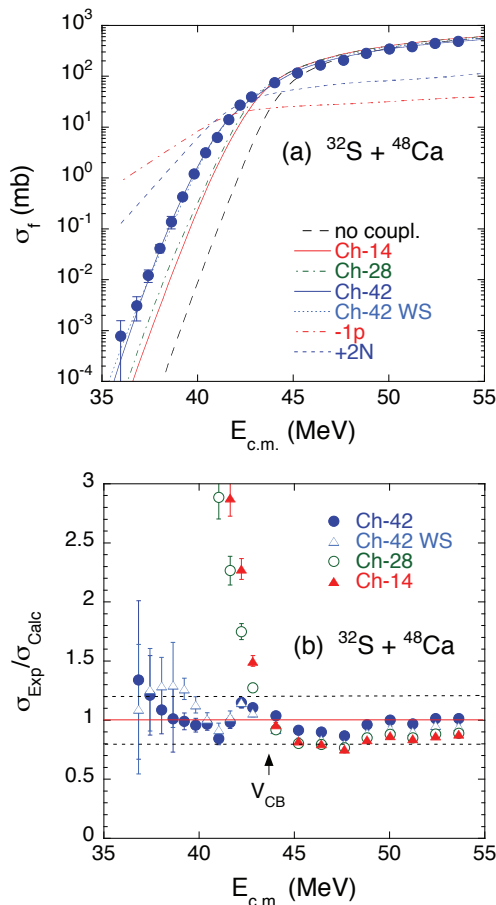


FIG. 6: (Color online) Fusion cross sections for $^{32}\text{S} + ^{48}\text{Ca}$ are compared to CC calculations based on the M3Y+repulsion potential. The calculation Ch-14 includes the surface excitations, Ch-28 takes into account, additionally, the one-proton transfer, and Ch-42 includes couplings to the one-proton and pair-transfer. Ch-1 is the no-coupling limit, and the result of the Ch-42 calculation using the WS potential is also shown. The predicted cross sections for one-proton (1P) and two-nucleon transfer (2N) are reported. The lower panel (b) shows the ratio of the measured and calculated cross section.

of $K = 230.6$ MeV.

V. ANALYSIS OF $^{36}\text{S} + ^{48}\text{Ca}$ FUSION DATA

The CC calculations for $^{36}\text{S} + ^{48}\text{Ca}$ include couplings to the excitation of all of the states shown in Table I, and also to the mutual excitations of the one-phonon states. The two-quadrupole-phonon excitation in ^{48}Ca was also considered, but a similar excitation could not be determined for ^{36}S and was therefore ignored. The energies and adopted $B(E2)$ values of the three members of the two-phonon triplet in ^{48}Ca have been combined into one effective two-phonon excitation (2PH(2^+)), see Refs. [22, 24]. That results in a total of 17 coupled channels and the calculation is referred to as Ch-17. This

includes the effect, above the barrier, of the weak imaginary potential of Eq.(1).

The best fit to the data of Ref. [12] is constructed by adjusting the radius of the ^{36}S matter density for each value of the diffuseness a_r , and the value of a_r that gives the absolute smallest value of the χ^2/N determines the best solution. A characteristic feature of this analysis is that there are two solutions that minimize the χ^2 . One solution has a small value of $a_r = 0.375$ fm and a small density radius. The other solution has $a_r = 0.427$ fm and a larger radius. The parameters of the two potentials, Sol-1 and Sol-2, are shown in Table II. The parameters of the density for the two solutions and the rms radii they produce are shown in Table III. The rms radii are seen to be smaller than the measured rms charge radius but they are close to the value of the point-proton rms radius.

The two entrance-channel M3Y+repulsion potentials are shown in Fig. 4. Also shown is a standard Woods-Saxon (WS) potential that provides an optimum fit to the $^{36}\text{S} + ^{48}\text{Ca}$ fusion data at energies above the Coulomb barrier. It has the diffuseness $a = 0.654$ fm, radius $R_{ws} = 8.143$ fm, and depth $V_0 = -63.45$ MeV. The barrier heights of the three potentials are essentially the same but the barriers of the two M3Y+repulsion potentials are thicker than the barrier produced by the standard WS potential. In the following only the solution with the larger radius and the shallow pocket (Sol-2) will be considered, since it gives the smallest χ^2/N and, more importantly, the rms radius of ^{36}S is too small for Sol-1, see Table III.

The calculated cross sections for the fusion of $^{36}\text{S} + ^{48}\text{Ca}$ are compared to the data [12] in Fig. 5(a). While the CC calculation based on the Sol-2 potential gives an excellent fit to the data, the calculation based on the WS potential exceeds the data at low energies. This is evidence of the fusion hindrance phenomenon, which is illustrated in Fig. 5(b) in terms of the ratio of the measured and calculated cross sections. It is seen that the ratio for the WS potential drops quickly below 1 at energies below the Coulomb barrier, V_{CB} . This was, in fact, the evidence that was used in Ref. [33] to identify the fusion hindrance phenomenon for the first time.

VI. ANALYSIS OF $^{32}\text{S} + ^{48}\text{Ca}$ FUSION DATA

The fusion data for $^{32}\text{S} + ^{48}\text{Ca}$ are analyzed by CC calculations that include couplings to the excitation of all of the states shown in Table I, including the effective two-phonon quadrupole excitations in ^{32}S and ^{48}Ca and the mutual excitations of the one-phonon states in projectile and target, whereas mutual excitations within the same nucleus (e.g., the 2^+ and 3^- states in ^{32}S) are ignored for computational reasons. That gives a total of 14 channels (Ch-14). It should be emphasized that ^{32}S is treated as a deformed nucleus using the quadrupole deformation parameter $\beta_2 = 0.315$ [23, 24]. The nucleus ^{36}S , on the other hand, is assumed to be spherical. The only param-

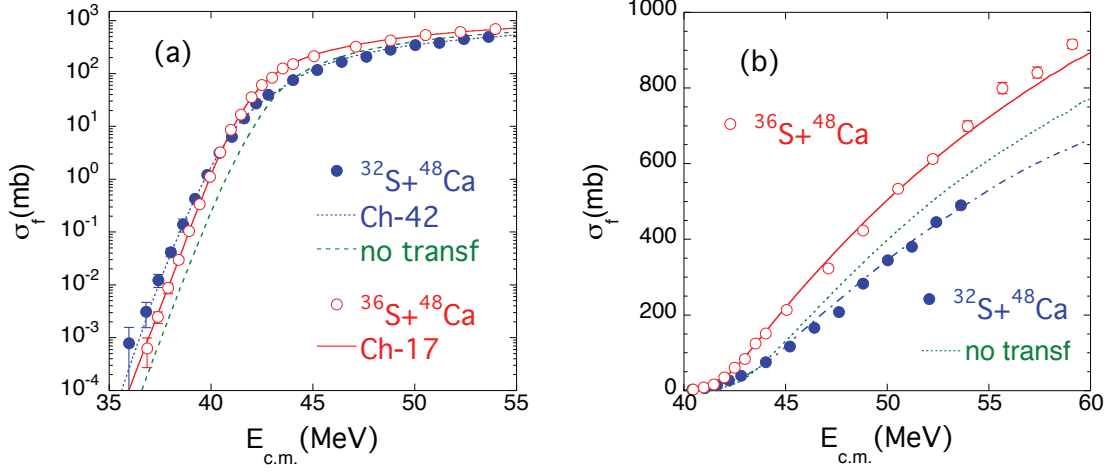


FIG. 7: (Color online) Logarithmic (a) and linear plot (b) of the fusion cross sections for $^{36}\text{S}+^{48}\text{Ca}$ [12] (open symbols) and $^{32}\text{S}+^{48}\text{Ca}$ (full symbols), compared to each other and to the full CC calculations. The calculation for $^{32}\text{S}+^{48}\text{Ca}$ without transfer coupling (no transf) is also shown.

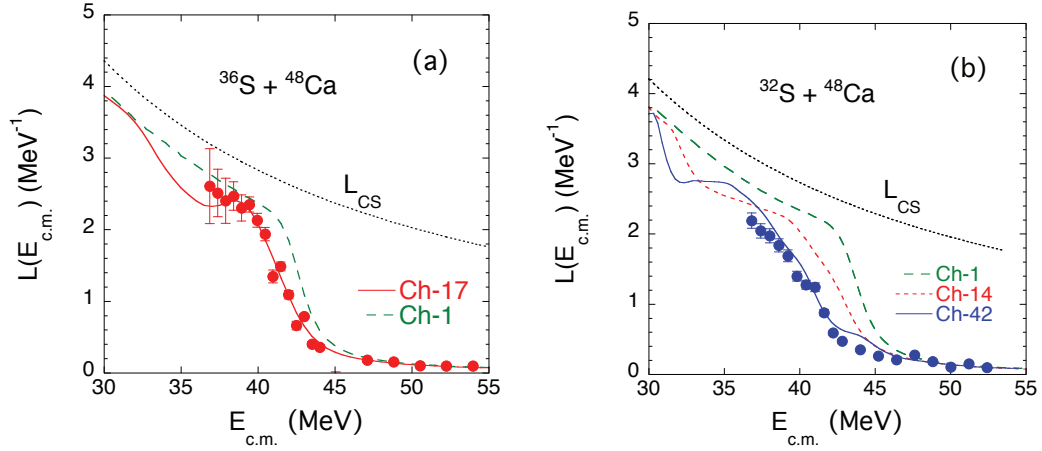


FIG. 8: (Color online) Logarithmic derivatives $L(E)$ of the (energy-weighted) cross sections shown in Fig. 7. The constant S factor limit L_{CS} is also indicated.

eter of the M3Y+repulsion potential is the radius of ^{32}S because the diffuseness associated with the repulsion is taken from the analysis of the $^{36}\text{S}+^{48}\text{Ca}$ fusion data. The parameters of the ^{32}S density are shown in Table III. It turns out that the rms radius is smaller than the value obtained for point-protons, even when the small effect of deformation is included.

The analysis of the $^{32}\text{S}+^{48}\text{Ca}$ fusion data also includes couplings to one- and two-nucleon transfer channels. The transfer channels were included in the calculations the same way it was done in Ref. [34], namely, by assuming that excitations and transfer can be treated as independent degrees of freedom (see Fig.1 of Ref. [34].) This assumption leads to a total of $3 \times 14 = 42$ channels when the one- and two-nucleon transfer are included, and the calculation is denoted Ch-42. The influence of one-nucleon transfer is dominated by one-proton transfer be-

cause the ground state Q -value is positive. The effect is simulated by applying the so-called Quesada form factors [35] which are implemented as described in Ref. [36]. The spectroscopic factors for proton transfer are the same as those used in Refs. [4, 9]. The effect of two-nucleon pair-transfer is simulated by the form factor [37],

$$F_t(r) = -\sigma_t \frac{dU(r)}{dr}, \quad (2)$$

where $U(r)$ is an ion-ion potential of the WS type. The parameters chosen here are $U_0 = -61.81$ MeV, $R = 7.94$ fm, and $a = 0.65$ fm (see below in this Section). The strength σ_t as well as the Q -value of the pair transfer are treated as adjustable parameters. The best fit is achieved with an effective Q -value of 1 MeV (as in Refs. [4, 38]); the optimum value of the transfer strength in Eq.(2) is $\sigma_t = 0.42$ fm.

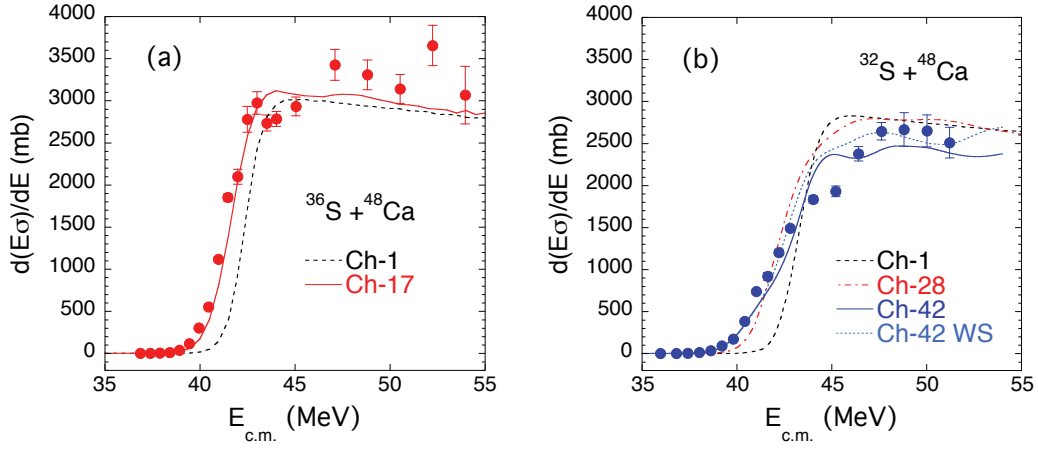


FIG. 9: (Color online) First derivative of the energy weighted fusion cross sections shown in Fig. 7.

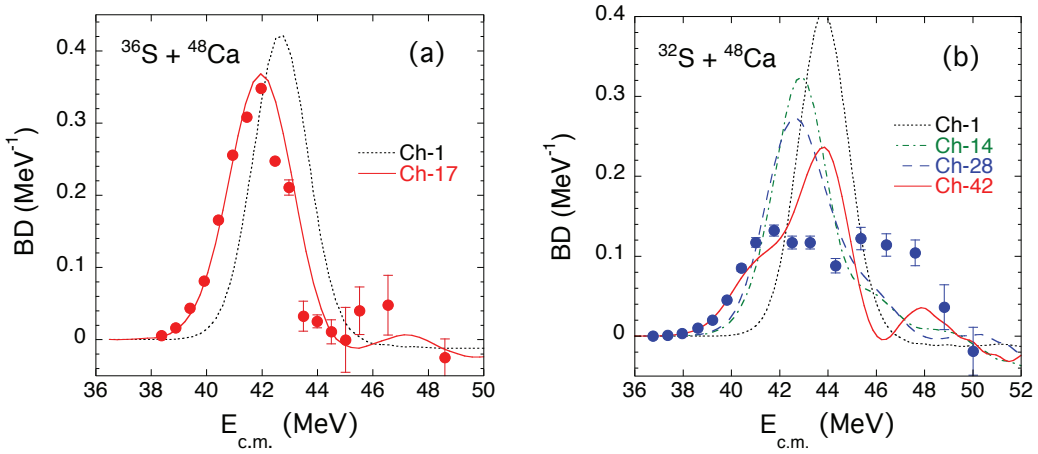


FIG. 10: (Color online) Barrier distributions $B(E)$ obtained as the second derivative of the energy-weighted cross sections shown in Fig. 7. The experimental distributions were obtained with the ΔE shown in the figures; the calculated distributions were obtained with $\Delta E = 1.5$ MeV.

The parameters of the M3Y+repulsion potential for $^{32}\text{S}+^{48}\text{Ca}$ are shown in Table II. The χ^2/N is 1.48, which is worse than the value achieved in fitting the $^{36}\text{S}+^{48}\text{Ca}$ data. This entrance channel potential is shown in Fig. 4 (bottom panel); it is similar to the shallow entrance channel potential for $^{36}\text{S}+^{48}\text{Ca}$ (top panel).

The calculated cross sections for the fusion of $^{32}\text{S}+^{48}\text{Ca}$ are compared to the data in Fig. 6(a). The calculations show the no-coupling limit (Ch-1), the calculation Ch-14 that includes couplings to surface excitation modes, the calculation Ch-28 taking into account, additionally, the one-proton coupling, and the full calculation Ch-42 that includes couplings to one-proton and pair-transfer. It is seen that the couplings to the transfer channels are crucial for obtaining a good fit to the data. The figure also shows the predicted one-proton and two-nucleon cross sections for $^{32}\text{S}+^{48}\text{Ca}$, marked with 1P and 2N, respectively. One-proton stripping cross sections, while being much larger below the barrier, become smaller than the two-nucleon transfer at high energies. A

”crossing” is calculated near the Coulomb barrier. One sees from Fig. 6(a) that the predicted pair-transfer cross section is about 100 mb at 10 MeV above the Coulomb barrier.

The effect of transfer on fusion is dominated by the pair transfer below the barrier. This can be seen in Fig. 6(b) where the ratio of measured and calculated cross sections is displayed. Here the ratio for the calculation Ch-28, which includes couplings to excitations of surface modes and the one-proton transfer, does not differ much from the calculation Ch-14, and both increase dramatically at energies below the Coulomb barrier, V_{CB} . The calculation Ch-42, which also includes the effect of pair transfer, is in much better agreement with the data since the ratio stays close to 1. The agreement with the data is not perfect because the ratio is slightly less than one just above the Coulomb barrier and it is slightly above one by 10-20% at energies just below the Coulomb barrier. A similar but less pronounced trend can be seen in Fig. 5(b) for the fusion of $^{36}\text{S}+^{48}\text{Ca}$.

A CC calculation (Ch-42) based on a WS potential has been performed also for $^{32}\text{S}+^{48}\text{Ca}$, in analogy with the case of $^{36}\text{S}+^{48}\text{Ca}$, using the potential parameters listed above in this Section just below Eq.(2). The parameters were chosen so to produce an optimum fit near the barrier. The results are compared to the data and to the analysis based on the M3Y+repulsion potential in Fig 6(a). It is seen that both calculations give a very good account of the excitation function, even if the WS potential gives a worse $\chi^2/N = 4.1$. This is evidence that the fusion hindrance phenomenon does not show up for $^{32}\text{S}+^{48}\text{Ca}$ in the measured energy range. Indeed, the plot of Fig 6(b) reveals in more detail that a clear-cut discrimination between the two potentials cannot be obtained by the sub-barrier behavior of the excitation function. Hindrance might appear at lower energies.

This behavior is different from what was observed for $^{40}\text{Ca}+^{48}\text{Ca}$ [4], where the slope of the excitation functions increases sharply at the level of $\simeq 20\mu\text{b}$, see Fig.7 of Ref. [4]. The underlying reason is presently not clear. It may depend on the different structure of ^{32}S and ^{40}Ca , or on details of transfer couplings.

VII. COMPARISON OF THE TWO SYSTEMS

The data sets for the two systems and the corresponding calculations are compared in Fig. 7. Besides the effect of transfer, it should be pointed out that the coupling to the quadrupole states is much stronger in the ^{32}S than in the ^{36}S induced reaction, whereas the coupling to the octupole states in the two sulphur isotopes are similar.

Fig. 7 shows the two fusion excitation functions, with logarithmic (a) and linear (b) scales of the cross sections. The agreement of calculations with data is quite good in the whole energy range. Without transfer couplings (the short-dashed curve), the data for $^{32}\text{S}+^{48}\text{Ca}$ would be underestimated below the barrier and overestimated above it. However, the effect of transfer is so strong that it enhances the cross sections to exceed the $^{36}\text{S}+^{48}\text{Ca}$ data at sub-barrier energies. At energies above the barrier, the $^{32}\text{S}+^{48}\text{Ca}$ cross sections are smaller than the $^{36}\text{S}+^{48}\text{Ca}$ fusion data. This situation is analogous to what was recently observed for the fusion of $^{40}\text{Ca}+^{48}\text{Ca}$ [4] where, however, hindrance does show up at the lowest measured energies.

The logarithmic derivatives of the energy weighted cross sections are shown in Fig. 8. One notes the tendency of the slope of the $^{36}\text{S}+^{48}\text{Ca}$ data to saturate at the lowest energies, as observed in Ref. [12], below the L_{CS} value. The same is not true for $^{32}\text{S}+^{48}\text{Ca}$, where the slope keeps increasing (slowly) with decreasing energy, even farther below the L_{CS} value. These features are well reproduced by the calculations that, in particular, predict a local maximum of the slope around 38 MeV for $^{36}\text{S}+^{48}\text{Ca}$. The analogous structure for $^{32}\text{S}+^{48}\text{Ca}$ is calculated to appear at still lower energies, where the cross section would be undoubtedly very small and very

difficult to measure.

The two panels of Fig. 9 report the first derivative of the energy weighted fusion cross section for the two systems. That quantity is proportional to the s-wave transmission coefficient T_0 , within some model restrictions [39]. In the case of $^{36}\text{S}+^{48}\text{Ca}$ we have essentially a step function, and the CC calculation nicely reproduces this structure. For $^{32}\text{S}+^{48}\text{Ca}$, " T_0 " increases more slowly from below to above the barrier. These trends become even more clear when considering the barrier distributions.

Indeed, the measured barrier distribution for $^{36}\text{S}+^{48}\text{Ca}$ (see Fig. 10(a)) consists of a strong narrow peak and a much weaker and broad structure at higher energies. These features are reproduced by the calculation Ch-17. The calculated peak is shifted about 1 MeV below the peak of the barrier distribution obtained from the one-dimensional calculation Ch-1. The measured barrier distribution for $^{32}\text{S}+^{48}\text{Ca}$ (see Fig. 10(b)), is very broad with at least two main peaks. The calculated distribution does not agree so well with the measured one. By comparing the Ch-14 and Ch-42 calculations it is anyway clear that it is the coupling to the transfer channels that is responsible for the broad barrier distribution.

A possible reason why the calculated barrier distribution for $^{32}\text{S}+^{48}\text{Ca}$ does not agree so well with the measured one could be that the transfer is simulated by a single effective transfer channel for one-proton transfer and another effective channel for the two-nucleon transfer. A better description would be to include transfer channels with a more realistic and broader range of Q -values. However, that is not obvious within the framework of the present model [34], where the transfer and surface excitations are assumed to be independent degrees of freedom.

VIII. SUMMARY

The fusion excitation function of $^{32}\text{S}+^{48}\text{Ca}$ has been measured in a wide energy range, down to very low energies where fusion cross sections are as low as $\simeq 800$ nb. The fusion cross section decreases smoothly below the barrier, and the logarithmic slope increases slowly and remains well below the L_{CS} value. No maximum of the astrophysical S factor is therefore observed.

The existing fusion data for $^{36}\text{S}+^{48}\text{Ca}$ [12] and the present ones for $^{32}\text{S}+^{48}\text{Ca}$ are analyzed by CC calculations that are based on the M3Y+repulsion, double-folding potential. The fusion data for $^{36}\text{S}+^{48}\text{Ca}$ [12] can be reproduced very well by considering couplings to low-lying states and mutual excitations of these states in projectile and target. This requires, however, some adjustments of the ion-ion potential. To explain the fusion data for $^{32}\text{S}+^{48}\text{Ca}$ it is necessary to consider the influence of the coupling to the (two-proton and two-neutron) pair-transfer channels with positive Q -values. This is in close analogy with the previously studied cases of the Ca+Ca

and Ni+Ni systems. The necessary strength predicts a pair-transfer cross section for $^{32}\text{S}+^{48}\text{Ca}$ of about 100 mb at 10 MeV above the Coulomb barrier. A measurement of transfer cross sections for this system would be desirable.

The barrier distribution extracted from the $^{32}\text{S}+^{48}\text{Ca}$ data is very wide and has two main peaks on either side of the unperturbed barrier. This peculiar shape is not well reproduced by calculations, even if the width of the distribution can only be reproduced by including transfer couplings in the calculations. We feel that a more realistic and detailed treatment of transfer couplings (two-nucleon transfer, in particular), might reduce the disagreement. At present, however, the double-peak structure of the barrier distributions remains unexplained to a large extent.

The hindrance phenomenon is observed for $^{36}\text{S}+^{48}\text{Ca}$, however, this is not true for $^{32}\text{S}+^{48}\text{Ca}$, where the data are well reproduced also by CC calculations employing a standard WS potential. The calculations suggest that this is mainly due to couplings to the transfer channels with positive Q -values, but the obvious difference with respect to the similar $^{40}\text{Ca}+^{48}\text{Ca}$ case shows that a com-

pletely satisfactory picture of sub-barrier fusion dynamics in these medium-light systems is not yet at hand.

IX. ACKNOWLEDGEMENTS

We acknowledge the highly professional work of the XTU Tandem staff during the beam times, and of M.Loriggiola for excellent target preparation. The research leading to these results has received funding from the European Union Sixth Framework Programme FP6 under the EURONS Contract (No. RII3-CT-2004-506065) and the European Union Seventh Framework Programme FP7/2007- 2013 under Grant Agreement No. 262010 - ENSAR. This work was also partly supported by the Croatian Ministry of Science, Education and Sports (Grant No. 0098-1191005-2890). C.L.J., H.E. and K.E.R. are supported by the U.S. Department of Energy, Office of Nuclear Physics, contract no. DE-AC02-06CH11357. X.D.T. is supported by the NSF under Grant No. PHY-0758100 and PHY-0822648, and the University of Notre Dame.

-
- [1] M. Beckerman *et al.*, Phys. Rev. C **25**, 837 (1982).
 - [2] M. Beckerman *et al.*, Phys. Rev. Lett. **45**, 1472 (1980).
 - [3] R. A. Broglia, C. H. Dasso, S. Landowne, and A. Winther, Phys. Rev. C **27**, 2433 (1983).
 - [4] G. Montagnoli *et al.*, Phys. Rev. C **85** 024607 (2012).
 - [5] C. L. Jiang *et al.*, Phys. Rev. C **82**, 041601(R) (2010).
 - [6] H. Timmers *et al.*, Nucl. Phys. A **633**, 421 (1998).
 - [7] A. M. Stefanini *et al.*, Phys. Rev. C **73**, 034606 (2006).
 - [8] A. M. Stefanini *et al.*, Nucl. Phys. A **456**, 509 (1986).
 - [9] R. J. Tighe *et al.*, Phys. Rev. C **42**, 1530 (1990).
 - [10] G. Montagnoli *et al.*, Phys. Rev. C **82**, 064609 (2010).
 - [11] H.Q. Zhang *et al.*, Phys. Rev. C **82**, 054609 (2010).
 - [12] A. M. Stefanini *et al.*, Phys. Rev. C **78**, 044607 (2008).
 - [13] G. Montagnoli *et al.*, Proc. Int. Conf. NN2012 on Nucleus-Nucleus Collisions, eds. Bao-An Li and J. Natowitz, J. Phys. Conf. Series, to be published.
 - [14] G. Montagnoli *et al.*, Proc. Int. Conf. on Nuclear Structure and Dynamics II (Opatija, Croatia, July 9-13, 2012), eds. Tamara Niksic, Matko Milin, Dario Vretenar, Suzana Szilner, AIP Conf. Proc. **1491**, 377 (2012).
 - [15] S. Misiu and H. Esbensen, Phys. Rev. Lett. **96**, 112701 (2006); Phys. Rev. C **75**, 034606 (2007).
 - [16] S. Beghini *et al.*, Nucl. Instr. Meth. A **239**, 585 (1985).
 - [17] N. Rowley, G.R. Satchler and P.H. Stelson, Phys. Lett. B **254**, 25 (1991).
 - [18] Akyüz Ö and Winther Å, in Nuclear Structure and Heavy-Ion Physics, Proc. Int. School of Physics Enrico Fermi, 1981 Course LXXVII, Varenna, eds. R.A. Broglia and R.A. Ricci (North Holland, Amsterdam).
 - [19] C.L. Jiang *et al.*, Phys. Rev. C **69**, 014604 (2004).
 - [20] C.L. Jiang, B.B. Back, H. Esbensen, R.V.F. Janssens and K. E. Rehm, Phys. Rev. C **73**, 014613 (2006).
 - [21] C.L. Jiang, *et al.*, Phys. Rev. C **79** 044601 (2009).
 - [22] H. Esbensen, C. L. Jiang, and A. M. Stefanini, Phys. Rev. C **82**, 054621 (2010).
 - [23] N.J. Stone, At. Data Nucl. Data Tables **90**, 75 (2005).
 - [24] H. Esbensen, Phys. Rev. C **68**, 034604 (2003).
 - [25] H. de Vries, C.W. Jaeger, and C. De Vries, At. Data Nucl. Data Tables **36**, 495 (1987).
 - [26] A. M. Stefanini *et al.*, Phys. Lett. B **679**, 95 (2009).
 - [27] W. D. Myers and W. J. Swiatecki, Phys. Rev. C **57**, 3020 (1998).
 - [28] H. Esbensen and F. Videbaek, Phys. Rev. C **40**, 126 (1989).
 - [29] Evaluated Nuclear Structure Data Files, National Nuclear Data Center, Brookhaven National Laboratory, [<http://www.nndc.bnl.gov/>].
 - [30] S. Raman *et al.*, At. Data and Nucl. Data Tables **36**, 1 (1987).
 - [31] T. Kibédi and R. H. Spear, At. Data and Nucl. Data Tables **80**, 35 (2002).
 - [32] I. Angeli, At. Data Nucl. Data Tables **87**, 185 (2004).
 - [33] C. L. Jiang *et al.*, Phys. Rev. Lett. **89**, 052701 (2002).
 - [34] H. Esbensen, C.L. Jiang, and K.E. Rehm, Phys. Rev. C **57**, 2401 (1998).
 - [35] J. M. Quesada, G. Pollaro, R. A. Broglia, and A. Winther, Nucl. Phys. A **442**, 381 (1985).
 - [36] H. Esbensen and S. Landowne, Nucl. Phys. A **492**, 473 (1989).
 - [37] C. H. Dasso and A. Vitturi, Phys. Lett. B **179**, 337 (1986).
 - [38] H. Esbensen, S. H. Fricke, and S. Landowne, Phys. Rev. C **40**, 2046 (1989).
 - [39] A.B. Balantekin and N. Takigawa, Rev. Mod. Phys. **70**, 77 (1998).